NBSIR 87-3564

Structural Reliability and Damage Tolerance of Ceramic Composites for High-Temperature Applications

---

E. R. Fuller, Jr., T. W. Coyle, R. F. Krause, Jr. and T. J. Chuang

U.S. DEPARTMENT OF COMMERCE
National Bureau of Standards
Ceramics Division
Gaithersburg, MD 20899

April 1987

Issued June 1987

Prepared for
ment of Energy
gy
esearch & Technology Development
rgy Material Program

NBSIR 87-3564

STRUCTURAL RELIABILITY AND DAMAGE TOLERANCE OF CERAMIC COMPOSITES FOR HIGH-TEMPERATURE APPLICATIONS

E. R. Fuller, Jr., T. W. Coyle, R. F. Krause, Jr. and T. J. Chuang

U.S. DEPARTMENT OF COMMERCE
National Bureau of Standards
Ceramics Division
Gaithersburg, MD 20899

April 1987

Issued June 1987

Prepared for
U.S. Department of Energy
Fossil Energy
Advanced Research & Technology Development
Fossile Energy Material Program

U.S. DEPARTMENT OF COMMERCE, Malcolm Baldrige, *Secretary*
NATIONAL BUREAU OF STANDARDS, Ernest Ambler, *Director*

NBS-1 - STRUCTURAL RELIABILITY AND DAMAGE TOLERANCE OF CERAMIC COMPOSITES FOR HIGH-TEMPERATURE APPLICATIONS

Semi-Annual Progress Report
for the period October 1987 through March 1987 to the
US Department of Energy, Fossil Energy,
Advanced Research & Technology Development,
Fossil Energy Material Program
under Interagency Agreement
Contract #DE-AI05-800R206179

E. R. Fuller, Jr., T. W. Coyle, R. F. Krause, Jr.
and T.-J. Chuang

National Bureau of Standards
Institute for Materials Science and Engineering
Ceramics Division
Gaithersburg, MD 20899

INTRODUCTION

The achievement of higher efficiency heat engines and heat recovery systems requires the availability of high temperature, high performance structural materials. Structural ceramics, and more recently, ceramic matrix composites, have received particular attention for these applications due to their high strength, and corrosion and thermal shock resistance. Even with these positive attributes, improved reliability and extended lifetime under service conditions are necessary for structural ceramics to gain industrial acceptance. The problems with these materials are mechanical and chemical in nature and are enhanced by the fact that they are subjected to high temperatures, reactive environments and extreme thermal gradients.

With an objective of improved performance for heat engine/heat recovery applications, the NBS program on structural ceramics and ceramic composites addresses these problems through the determination of the critical factors which influence mechanical and microstructural behavior. The activities of the program are grouped under two major subtasks, each designed to develop key data, associated test methods and companion predictive models. The status of the subtasks are detailed in the following sections.

DISCUSSION OF CURRENT ACTIVITIES

SUBTASK A: INTERFACIAL AND MICROSTRUCTURAL COMPOSITE PROPERTIES

1.1 Measurement of Fiber/Matrix Interfacial Forces

Instrumented Indenter Testing

Introduction

A method based on the indentation technique of Marshall [1] has been developed to characterize the mechanical behavior of the fiber/matrix interface under applied shear loads. On a polished cross section of the specimen, a force is applied to a fiber parallel to the fiber axis, resulting in a displacement of the fiber relative to the matrix surface. To determine the resistance to shear displacement along the fiber/matrix interface it is necessary to know the force applied to the fiber, the relative displacement between fiber and matrix, and the area of interface over which the displacement occurs. A Vickers hardness indenter instrumented to measure the load applied to the specimen and the displacement of the tip of the diamond indenter is employed to apply the force to the fiber. The resulting load-displacement curves can then be used in conjunction with appropriate mechanics analyses to characterize the behavior of the interface.

Modelling

The experimentally obtained curves of applied load versus the displacement of the diamond indenter must first be corrected to give the desired force-displacement curves. During the initial portion of the loading curve the tip of the diamond penetrates the surface of the fiber while simultaneously the fiber begins to slip down into the matrix. To determine the displacement of the fiber surface relative to the surrounding matrix, (u), that part, (a), of the total displacement (δ) due to the penetration of the indenter into the fiber must be subtracted, i.e. $u=\delta-a$. Assuming that the hardness of the fiber is constant, independent of load or depth of penetration, this correction can be calculated from the definition

of hardness, the geometry of the indenter, the fiber hardness (H_f), and the applied load (P). With hardness defined as $H_f=2P/d^2$, where d is the diagonal length of the indentation in the fiber surface, the geometry of the indentation yields:

$$a = (F/2H_f)^{1/2}/\mathrm{Tan}\ \Phi \tag{1}$$

where a is the depth of the indentation relative to the fiber surface, F the force applied to the fiber, and Φ the half-angle of the Vickers indenter (74°). Initially all of the applied load acts on the fiber, ie. F = P. Later in the loading process as the fiber slips down into the matrix the edges of the indenter begin to penetrate the surrounding matrix. This begins when d = 2R or at a total displacement (δ) of:

$$\delta = R/\mathrm{Tan}\ \Phi \tag{2}$$

A portion of the load is now carried directly by the matrix and this must be subtracted from the measured load to obtain the force on the fiber.

The calculation of τ when the fiber slippage occurs through the entire thickness of the sample is relatively straightforward if it is assumed that the applied shear stress is constant along the interface (i.e. ignoring the stress concentration near the free surface). When τ is constant, a simple force balance yields:

$$\tau = F\ /\ 2\pi\ R\ t \tag{3}$$

where t is the thickness of the specimen. In this case the applied load should be independent of displacement for δ less than given by Eq. 2.

The calculation is more complicated when the sample thickness (t) is larger than the length of fiber over which slippage occurs (l). Marshall [1] has presented an approximate analysis for the case of t>>l. The following description of the expected force-displacement relationship is based on this analysis. Stress concentrations and Poisson's ratio effects are ignored, and τ is assumed to be constant, independent of position and slippage distance. During loading the displacement of the

fiber end involves slippage of the fiber relative to the matrix and a compression of the fiber over the length l. The value of τ can be obtained from the slope of a plot of F^2 versus u:

$$F^2 = \frac{4\pi^2 R^3 E_f}{[1 - \pi B(R/l)^2]^2}\tau u - \left[\frac{2\pi B(\tau/E_f)}{\{1 - \pi B(R/l)^2\}^3}\right] \qquad (4)$$

where E_f is the Young's modulus of the fiber and B a constant ($\approx$1) [1]. The terms in square brackets arise from consideration of the axial compressive stress in the fiber at l, the end of the sliding area. They become negligible when the length over which slippage is occurring is much greater than the fiber radius (l>>R). This criterion is satisfied for $u \gg 3\pi BR\tau/E_f$.

On unloading, the fiber extends back towards the surface to relieve the axial compressive stresses until, with F=0, these are balanced by the interfacial shear tractions. During unloading τ can be evaluated from the slope of a plot of $(\Delta F)^2$ versus Δu, where ΔF is the difference between the maximum applied force and the current level of applied force and Δu is similarly the difference between the displacement at maximum load and the current displacement:

$$(\Delta F)^2 = 8\pi^2 R^3 E_f \tau \Delta u \qquad (5)$$

where the terms corresponding to those in the square brackets in Eq. 4 have been omitted. Note that the slope given by Eq. 5 is twice that given by Eq. 4. The slippage which occurs on unloading is therefore half that which occurred during loading, so that when the fiber has been completely unloaded the residual displacement of the fiber below the matrix surface should be one-half of the displacement at maximum load.

Results and Discussion

A plot of F^2 versus u is shown in Fig. 1 for a Nicalon SiC fiber in a glass ceramic (LAS III) matrix[1]. As described in Eq. 4 the slope of this

---

[1] United Technologies Research Center, East Hartford, CT.

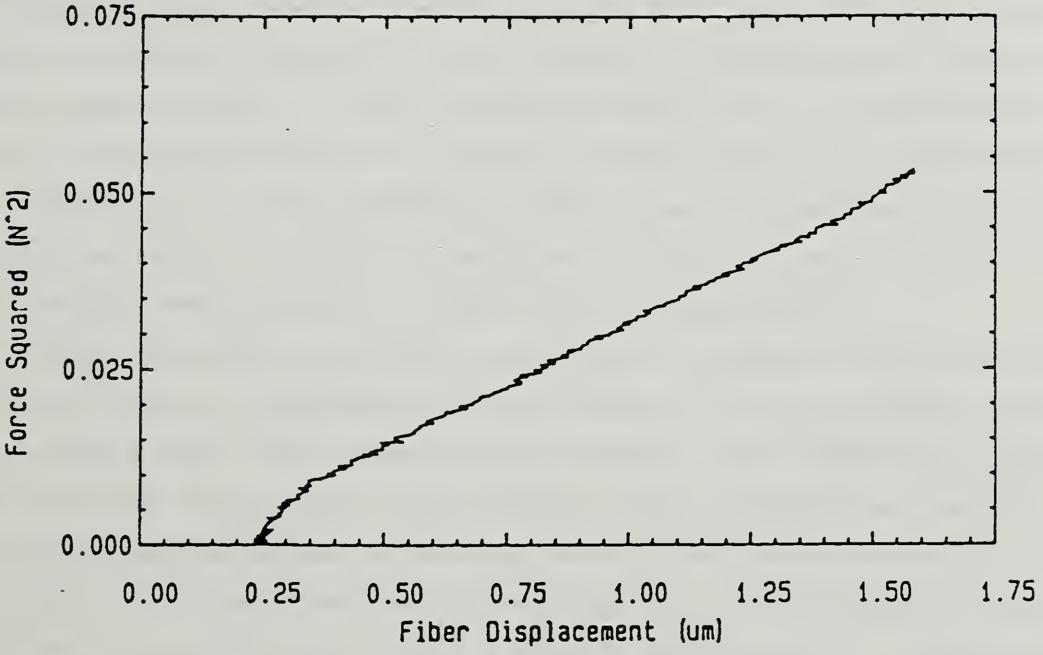

Figure 1. Plot of the square of the force applied to a fiber versus the displacement of the end of the fiber relative to the matrix surface during an instrumented indenter test. The fiber diameter is 17.0μm.

curve is proportional to τ over the range of u where the conditions $l \gg r$ and $d < 2R$ are satisfied. The curve is nearly linear over the range $0.25\mu m < u < 1.25\mu m$, with a slope of 3.41×10^4 N^2/m. The fiber radius, R, is $8.5\mu m$ and the modulus, E_f, 200 GPa. From Eq. 4 (ignoring the terms in square brackets) τ is given as 7.0 MPa, in good agreement with other measurements of τ in this system. At large u the non-linearity can be attributed to the indenter making contact with the surrounding matrix. The curve also shows a change in slope at small u, shown more clearly at a larger scale in Fig. 2. The bracketed terms in Eq. 4 become important at small u and would lead to an increase in the slope for a given constant τ, as observed. It is not possible at this time to quantitatively compare the projections of Eq. 4 with the detailed behavior at small u due to the experimental uncertainties at such small displacements.

Other considerations would also tend to increase the force required to cause the initial displacement of the fiber. If it is assumed that an area of interface must first debond before sliding, this debonding region would move from the surface down the interface into the bulk as loading continued, leaving behind a growing area of frictional contact. Thus the measured τ could be viewed as the average of a constant small area of relatively high effective τ and a growing area of low τ. Details of the stress distribution at the interface near the free surface become important when the assumptions of constant applied shear load along the interface and constant τ are relaxed. More sophisticated modelling and more precise experimental results are necessary before the behavior in this region near the initiation of fiber slippage is understood.

1.2 Characterization of Matrix Crack - Fiber Interactions

DCDC Fracture Specimens[2]

Introduction

A critical issue in the fracture behavior and mechanical performance of ceramic matrix composites is the influence of the strength of the

---

[2] The processing aspects of this work were conducted with support from the SDIO/IST program under ONR contract #N00014-86-F-0096.

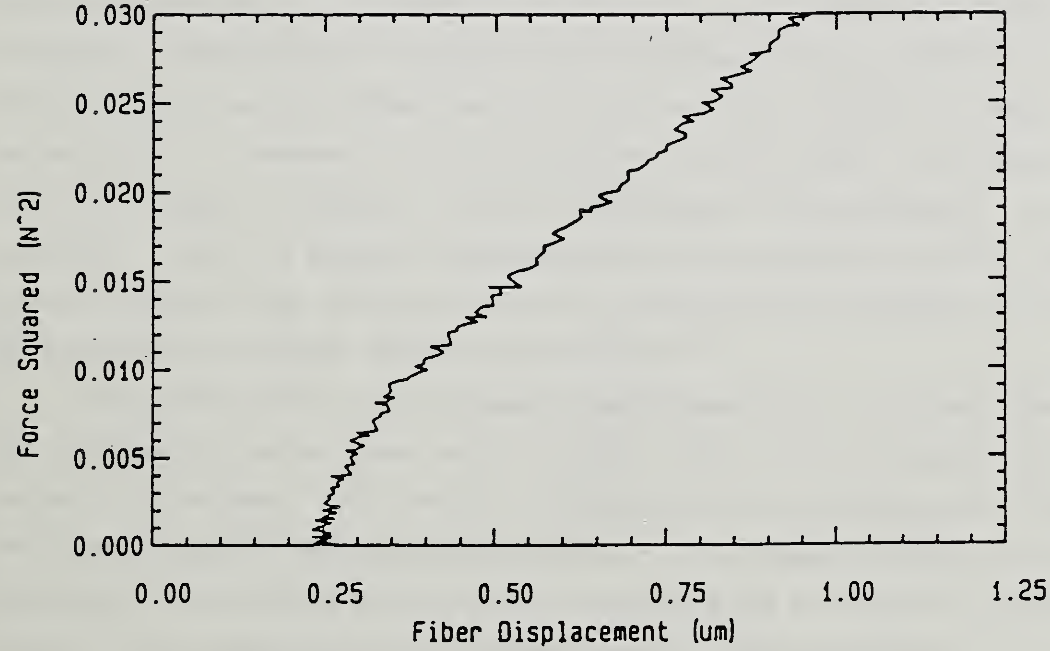

Figure 2. An expanded view of the low load, small displacement portion of the curve shown in Fig. 4 emphasizing the non-linearity of the behavior in this region.

fiber/matrix interface on the interaction of a crack with individual fibers. It is generally accepted that if a strong bond is present between fiber and matrix, transverse cracks run directly through the reinforcing fibers, which then have little effect on retarding propagation of the crack. Although the strength of such a composite may be enhanced through load transfer, the toughness is not appreciably improved and failure is completely brittle. A weak interface leads to crack deflection, debonding along the fiber/matrix interface and bridging of the crack by the fibers. If the fibers do not break behind the crack tip, failure is non-catastrophic. However, if the interface is too weak, the fibers slide freely through the matrix, and no improvement in strength or toughness is obtained. Thus, a better understanding of the details of this behavior is required before the optimum levels of interfacial strength can be determined for a given fiber-matrix system.

This issue can be investigated experimentally by direct observation of the interaction of a crack with a single fiber in an appropriate fracture mechanics specimen. The double cleavage drilled compression (DCDC) configuration [2] was employed because of the simple shape and loading geometry. No guiding side grooves are required to keep the plane of the crack in the center of this compressively loaded specimen.

Stable crack propagation is obtained in the DCDC specimen since the applied stress intensity (K_{app}) experienced at the crack tip decreases with crack extension at a constant load. From the measured crack length (c) at a given remotely applied compressive stress (σ_{app}), K_{app} can be calculated from an expression of the following form [2]:

$$K_{app} = \sigma_{app} \sqrt{r} \, / \, [(c/r) \, f(c/r)] \qquad (6)$$

where the specimen dimensions are as defined in Fig. 3. The function $f(c/r)$ can be determined experimentally by testing specimens of known K_{IC}. Fracture mechanics analyses of this specimen have been performed [2-4] and yield good agreement with the experimental results.

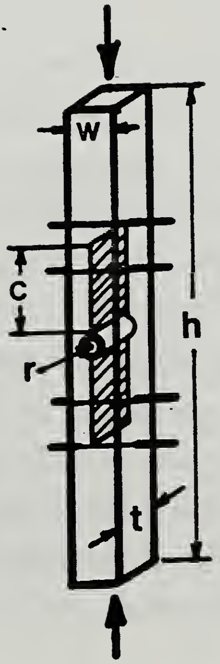

Figure 3. Double-cleavage drilled-compression fracture mechanics specimen. Compressive load opens cracks above and below centered hole.

Experimental Procedure

Transparent specimens were produced by sandwiching SiC fiber[3] between borosilicate glass plates[4] which were then fused together by heating in air at approximately 850°C for 10-15 min. to produce transparent specimens. The samples were loaded in compression with a screw-driven mechanical testing machine[5] at a crosshead displacement rate of 0.005 cm/min. The strain contours visible in cross-polarized illumination were used to monitor the length of the growing crack and to characterize the crack-fiber interactions.

Stress wave fractography [5] was utilized to monitor the shape of the crack front and the relative velocity of the growing crack along the specimen. Acoustic waves were propagated through the specimen during crack extension by use of a ceramic piezoelectric transducer coupled to the specimen. The transducer was driven with bursts of an 80-90 KHz sine wave at a maximum of 30 V peak to peak. The burst frequency was 5 Hz; the burst duration was 25% of the low frequency period. This technique produces ripples on the fracture surface at a spacing determined by the frequency of the acoustic excitation. These ripples can then be observed by optical microscopy in reflected light using Nomarsky contrast. With a constant excitation frequency, widely spaced bands indicate a region of rapid crack extension while closely spaced bands indicate relatively slow crack growth.

Results and Discussion

Direct, qualitative observations of several aspects of the fracture behavior in the specimen could be made in transmitted, cross-polarized illumination at various magnifications. Typically the fiber could be seen to bridge the crack for some distance behind the crack tip before breaking. Evidence of localized strain at the fiber-crack surface intersection (Fig. 4) indicated that the bridging fiber was applying tractions across the

---

[3] SCS-6 SiC Fibers, Avco Corp., Wilmington, MA.

[4] Corning 7740, Corning Glass works, Corning, NY.

[5] Instron Corp., Canton, MA.

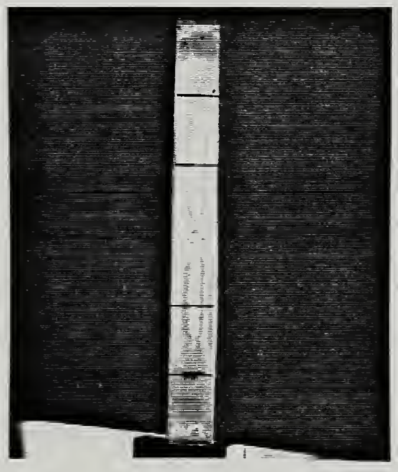

Figure 4. View perpendicular to fiber axes of DCDC specimen under load. The cracks are seen edge-on with the crack tips located between the inner and outer fibers. Strain contours are visible by virtue of the transmitted cross-polarized illumination.

crack faces. The shape of the strain contours ahead of the crack tip or behind the crack tip away from the crack surfaces gave only occasional faint indications of localized strain which would show load transfer to the fiber. Apparent delamination of the fiber ahead of the crack (Fig. 5) was observed when a higher magnification was used for one specimen.

An optical micrograph of a region of the fracture surface which includes a fiber, taken with Nomarsky contrast, is shown in Fig. 6. The light and dark bands visible under these conditions represent "snapshots" of the position and shape of the crack front at periodic intervals. It can be seen that the crack front bowed around the fiber which was bridging the crack before the center portion broke away and accelerated to reform a nearly straight front. A scanning electron micrograph of this area (Fig. 7) shows that after bowing around the fiber the two sides of the crack did not meet on the same plane. The resulting ligament would have to have fractured before the center portion of the crack front could extend. From the direct observations discussed above, the fiber appears to have broken at some later time, after the ligament had fractured and the crack front had moved well beyond the fiber. The chipping apparent around the fiber in Fig. 7 would have occurred as the broken fiber was pulled out of the glass matrix.

To quantitatively assess the influence of the fibers on the crack propagation, the crack length was measured from photographs, such as shown in Fig. 4, and used to calculate the apparent K_{app} from the applied load using Eq. 6. The results for several specimens are shown in Fig. 8. Assuming that the crack is growing at a constant stress intensity, $K_{tip} = K_{IC}$ for the glass matrix, the increase in the calculated K_{app} for crack lengths beyond the fiber position reflects the closure tractions exerted by the bridging fiber (K_{trac}).

$$K_{tip} = K_{IC} = K_{app} + K_{trac} \tag{7}$$

or

$$K_{trac} = K_{IC} - K_{app} \tag{8}$$

The stress intensity factor due to a point force acting at a distance δ behind the crack tip is given by [6]:

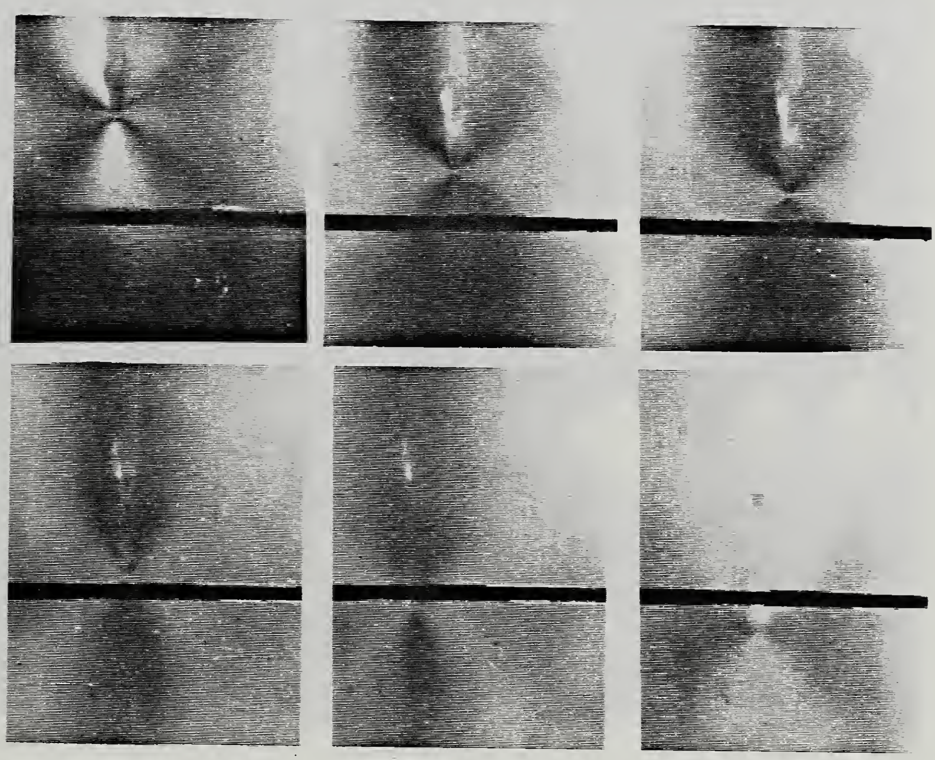

Figure 5. Higher magnification views in cross-polarized transmitted light of region near reinforcing fiber. Crack-tip is seen approaching and then passing the fiber as the remotely applied load is increased. Field of view is approximately 2.7mm wide.

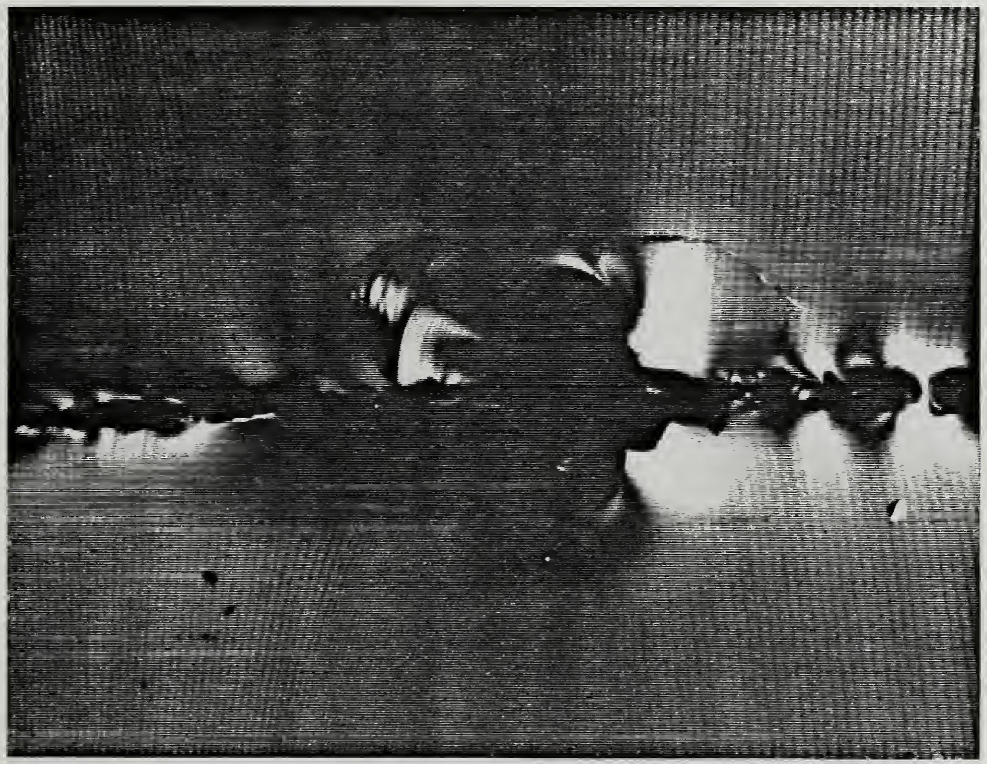

Figure 6. Optical micrograph of a region of the fracture surface centered about a reinforcing fiber. Nomarsky contrast reveals the periodic surface undulations caused by the applied acoustic waves. The crack was propagating from right to left. The field of view is approximately 1mm wide.

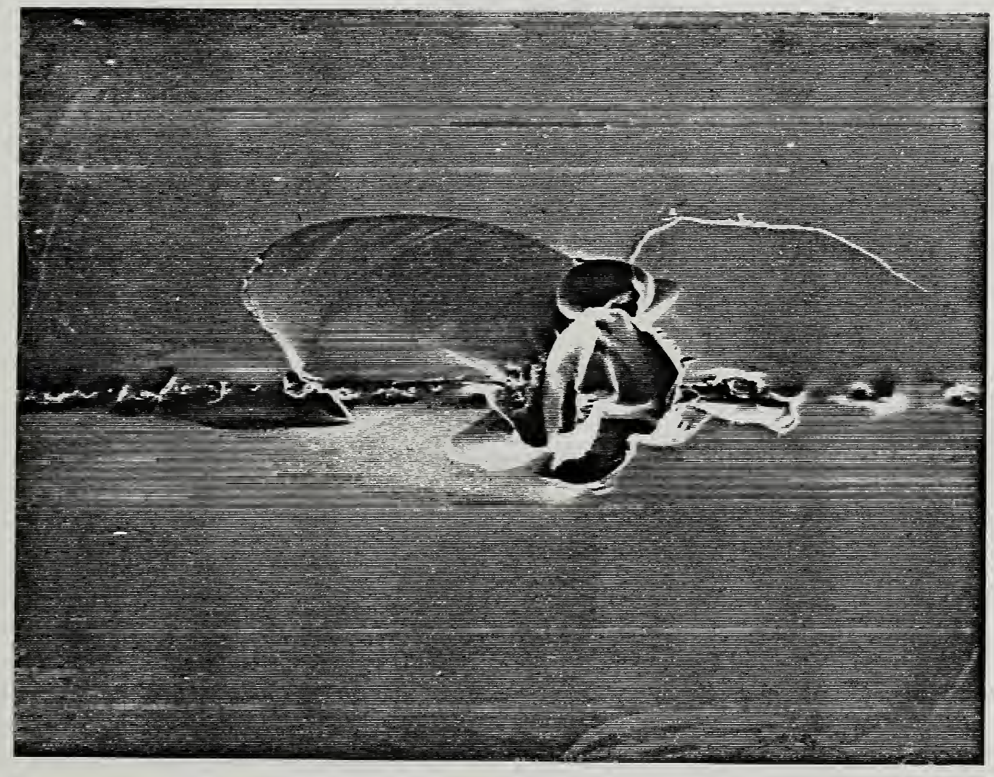

Figure 7. Scanning electron micrograph of area shown in Fig. 6. The remnant of the ligament formed as the crack front swept around the fiber can be seen to the left of the fiber. (Field of view approximately 1.1mm wide.)

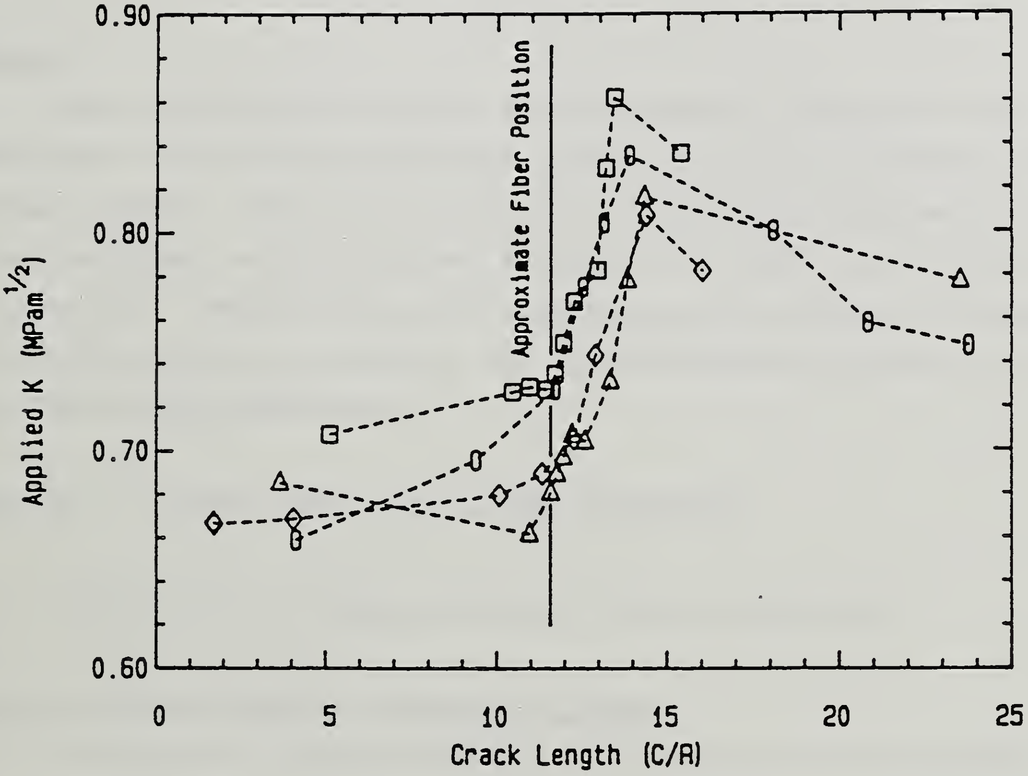

Figure 8. Plot of remotely applied K (calculated from Eq. 6) versus crack length showing relative position of the reinforcing fiber. Increase in the applied K required to propagate the crack reflects the closure forces exerted by the bridging fiber.

$$K_{trac} = -\sqrt{2}\, F / (\pi\, \delta)^{3/2} \qquad (9)$$

where the point force, F, may be a function of δ. Thus, information regarding the forces exerted by the bridging fiber as a function of crack length can be obtained from data such as shown in Fig. 8.

Summary

Sample fabrication methods and experimental techniques have been developed which allow crack-fiber interactions to be directly examined in a ceramic matrix. Qualitative information regarding fiber/matrix debonding, fiber bridging, and pinning and bowing of the crack front at the fiber can be obtained. Possibilities for quantifying the effects of bridging fibers on crack extension in terms of the tractions exerted across the crack by the fiber were demonstrated.

SUBTASK B: DAMAGE MODES AND FAILURE MECHANISMS

1.4. Elucidation of Damage Modes and Failure Mechanisms

Silicon Carbide Whisker Reinforced Alumina

The fracture toughness behavior of a silicon carbide whisker reinforced alumina ceramic has been characterized as a function of porosity. The alumina was hot pressed with 25 weight percent silicon carbide whiskers to form composite materials whose porosity ranged nominally from 1 to 11 percent. Controlled flaws of increasing size were produced on polished surfaces of specimens by Vickers indentation loading from 2 to 200 N. The flexure strength measured as a function of indentation load indicates that the resistance to fracture of these materials increases as a function of crack extension. Results are analyzable in terms of fracture models containing ligamentary tractions in the wake of the crack.

a. Experimental Procedure

Four billets of a silicon carbide whisker reinforced alumina ceramic, whose respective porosities ranged nominally from 1 to 11 percent, were provided for this investigation through the courtesy of J. F. Rhodes of ARCO Chemical Company [7,8]. A fine-grained alumina powder was hot pressed with 25 weight percent silicon carbide whiskers, 0.45 to 0.65 μm in diameter and 10 to 80 μm in length [9], to form billets of the composite material: 3 billets at 150 mm x 150 mm x 12 mm and a billet (nominally 1 percent porosity) at 100 mm diam x 15 mm. The silicon and carbon sources were rice hull ash and rice hull hydrocarbons, respectively [9].

Samples were diamond-sawed from the billets to fabricate flexure specimens, nominally 3 mm x 4 mm x 50 mm, with the prospective tensile surface, 4 mm x 50 mm, normal to the hot-press direction. The sides of the specimens were diamond-grounded flat and parallel within 30 μm. The prospective tensile surfaces of the flexure specimens were polished with 9 μm diamond paste. The specimens were soaked and rinsed in ethyl alcohol and dried in a hot air flow.

The porosity, p, of a flexure specimen was calculated by

$$p = 1 - \rho_b/\rho_t \tag{10}$$

where ρ_b and ρ_t are the bulk and theoretical densities, respectively. The bulk density, ρ_b, was determined from the mass and bulk dimensions of the specimen. The theoretical density, $\rho_t = 3.762$ g/cm^3, was calculated from

$$1/\rho_t = w_1/\rho_1 + w_2/\rho_2 \tag{11}$$

where w_i is the weight fraction and ρ_i is the X-ray density of the ith component: $\rho_1 = 3.987$ g/cm^3 for Al_2O_3 and $\rho_2 = 3.217$ g/cm^3 for SiC.

A flaw of variable size, controlled by Vickers indentation loading between 2 N and 200 N, was placed in the center of the prospective tensile surface of several of the flexure specimens. Care was taken to orient one set of the radial cracks of an indentation flaw in the direction of prospective rupture. The indentations were made in air at room temperature with a steady loading rate that required 15 s to produce a full load. The

diamond pyramid contacted the specimen surface for about 30 s before it was withdrawn to complete the load cycle. The lengths of surface cracks were measured by optical microscopy, using a calibrated scale accurate within 2 μm.

Strength tests were conducted on specimens under 4-point flexure in dry nitrogen at room temperature. The gear-driven crosshead of a universal testing machine was operated at a constant load-point displacement speed of 5 mm/min, producing a loading rate of 145 N/s on the material, until the applied load attained its maximum value, F, required to rupture the specimen. The load was transmitted to the specimen through 6 mm diameter rollers. Loading was measured by a linear load transducer and was recorded on a constant speed chart. The load transducer was calibrated at the full scale of the chart with a known 10 kg mass, which was converted to force units by the local acceleration of gravity, 9.801 m/s^2. The flexure strength, S, was calculated from

$$S = 3(\ell_1 - \ell_2)F/2BW^2 \qquad (12)$$

in which the loading spans were $\ell_1 = 40$ mm and $\ell_2 = 10$ mm and in which the nominal dimensions of the specimen were B = 4 mm and W = 3 mm. Following rupture of a specimen, it was examined by optical microscopy to confirm whether or not the fractured surface passed through a radial crack of the indentation flaw.

b. Data Analysis

According to the energy principle, incremental crack extension, dc, can occur when the applied stress-intensity factor, K, is equal to or greater than the crack-extension resistance of the material, K_R. The criterion for the onset of crack-extension instability, leading finally to failure, is the point of tangency,

$$dK/dc = dK_R/dc \qquad (13)$$

An equilibrium position will be attained at $K = K_R$, if $dK/dc < dK_R/dc$.

When a sufficient load, P, is applied to a sharp indenter in contact with a material and the indenter is then unloaded, semi-circular radial cracks, c_I, will develop in the material [10]. The driving force of the crack system may be characterized by a residual stress-intensity factor,

$$K_r = \chi P c^{-3/2} \qquad (14)$$

where χ is a constant dependent on the material and indenter geometry.

When a freshly-indented material is subjected to a small bending stress, σ, a bending stress-intensity factor, K_b, will be superposed upon K_r. The crack system will grow as long as $(K_r + K_b) \geq K_R$. The bending stress-intensity factor may be expressed as

$$K_b = Y \sigma c^{1/2} \qquad (15)$$

where Y is a configuration coefficient which is dependent on specimen and flaw geometry. Catastrophic failure ensues when the criterion of Eq. (13) is satisfied. This condition occurs when $\sigma = S$.

To facilitate analysis of the data, a parametric representation of the fracture resistance as a power-law function in crack extension is used [11]:

$$K_R = K_o (c/c_o)^{1/r} \qquad (16)$$

where K_o and c_o are constants, and r^{-1} is a constant which measures the susceptibility to R-curve behavior (i.e., the susceptibility for a rising fracture resistance with crack extension). When $r^{-1} = 0$, Eq. (16) gives completely brittle behavior with $K_R = K_o = K_{IC}$. Using Eq. (16), a solution of the fracture mechanics equations gives [11]

$$S = CP^{-b} \qquad (17)$$

in which the R-curve susceptibility is given by

$$r^{-1} = (1 - 3b)/(2+2b) \qquad (18)$$

and the coefficient of crack-extension resistance is given by

$$K_o = YC(Ab)^{-b} (1 + b)^{(1+b)} c_o^{1/r} \tag{19}$$

When $K_r = K_R$, the coefficient A is defined in terms of the initial indentation flaw size, c_I, as

$$A = K_o/\chi c_o^{1/r} = P/c_I^{2/(1+b)} \tag{20}$$

c. Experimental Results

Thus far only two of the four billets of the whisker-reinforced alumina ceramic have been characterized. Table 1 gives the mean porosity, p, and the standard deviation of the mean from measurements on 24 flexure specimens from each of the two billets. In general, specimens from the edges of the billets tended to be slightly less porous.

Figure 9 shows the bending strength as a function of indentation load for the selected porosities of the material. A straight line, the logarithm of Eq. (17), was fitted by a method of least squares to evaluate the coefficients b and C for each porosity. Table 1 gives these values and their standard deviations. Only those indentation loads which correspond to the fractured surface having passed through a radial crack of an indentation flaw are considered valid points for the fit. The open circles which are arbitrarily plotted at $\log_{10}(P) = 0$ correspond to strengths of non-indented specimens. A plateau of strength which is invariant with indentation load exists over a region of small indentation flaws for each porosity, but the range of this plateau decreases with decreasing porosity of the material. An estimate of effective size of intrinsic flaws of a selected porosity could be made by the intersection of a plateau line with the straight line of the least-squares-fit. The dashed line describes a slope of -1/3, which would indicate a fracture toughness invariant with crack size, as would be expected in the region of large crack size.

Figure 10 shows the half-length of surface crack as a function of indentation load for the selected porosities of the material. The dashed line is a least-squares-fit to the observed data. In principle an alternate value of b could be deduced from the slope of this fit, (1+b)/2.

Table 1. Values of parameters that define crack-extension resistance, K_R, of a 25 wt percent silicon carbide whisker reinforced alumina ceramic at various porosities. The uncertainty for each value is its standard deviation.

Parameter[a]	Billet 1	Billet 3
A. Porosity		
p, percent	11.48 ± 0.16	4.89 ± 0.14
Number of measurements	24	24
B. Indentation Crack Length		
$\log_{10}(A)$	8.0447 ± 0.0243	8.1645 ± 0.0212
$\chi = K_o/Ac_o{}^{1/r}$	0.095	0.088
Number of measurements	6	6
C. Bending Strength of Indented Beams		
b	0.2759 ± 0.0148	0.2657 ± 0.0093
$\log_{10}(C)$	2.8808 ± 0.0265	2.9258 ± 0.0149
Number of measurements	13	18
Student's t, 90 percent confidence band	1.363	1.337
D. Crack-Extension Resistance		
r	14.8 ± 4.0	12.5 ± 1.8
K_o in $\mathrm{MPa \cdot m^{1/2}}$	4.12 ± 0.46	4.24 ± 0.37

---

[a] Calculations correspond to P in N, C in M, S in MPa and $C_o = 1\mu m$

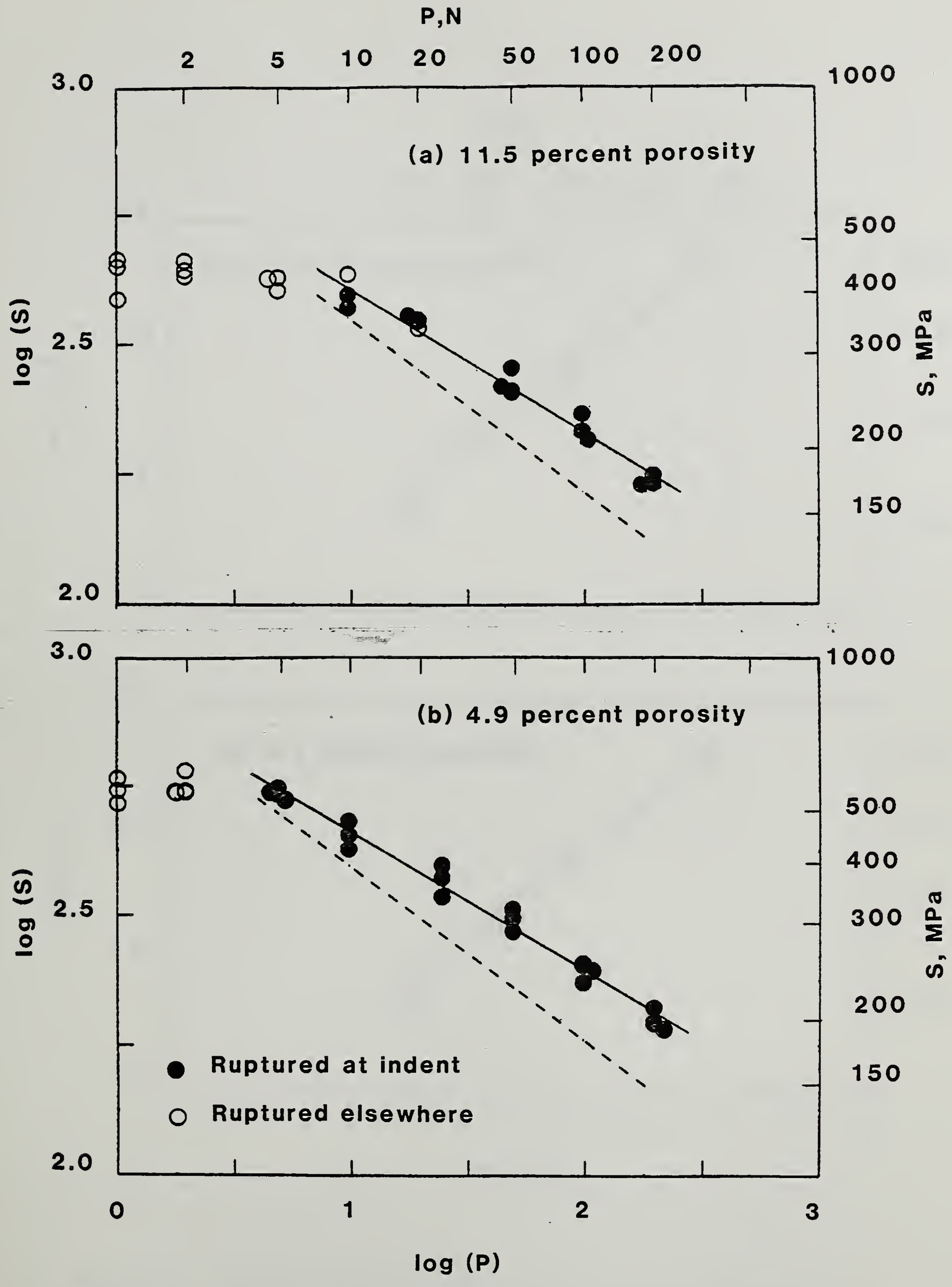

Figure 9. Bending strength, S, as a function of indentation load, P, for silicon carbide whisker reinforced alumina ceramics at selected porosities. The solid line is a least-squares-fit, and the dashed line describes a slope of -1/3.

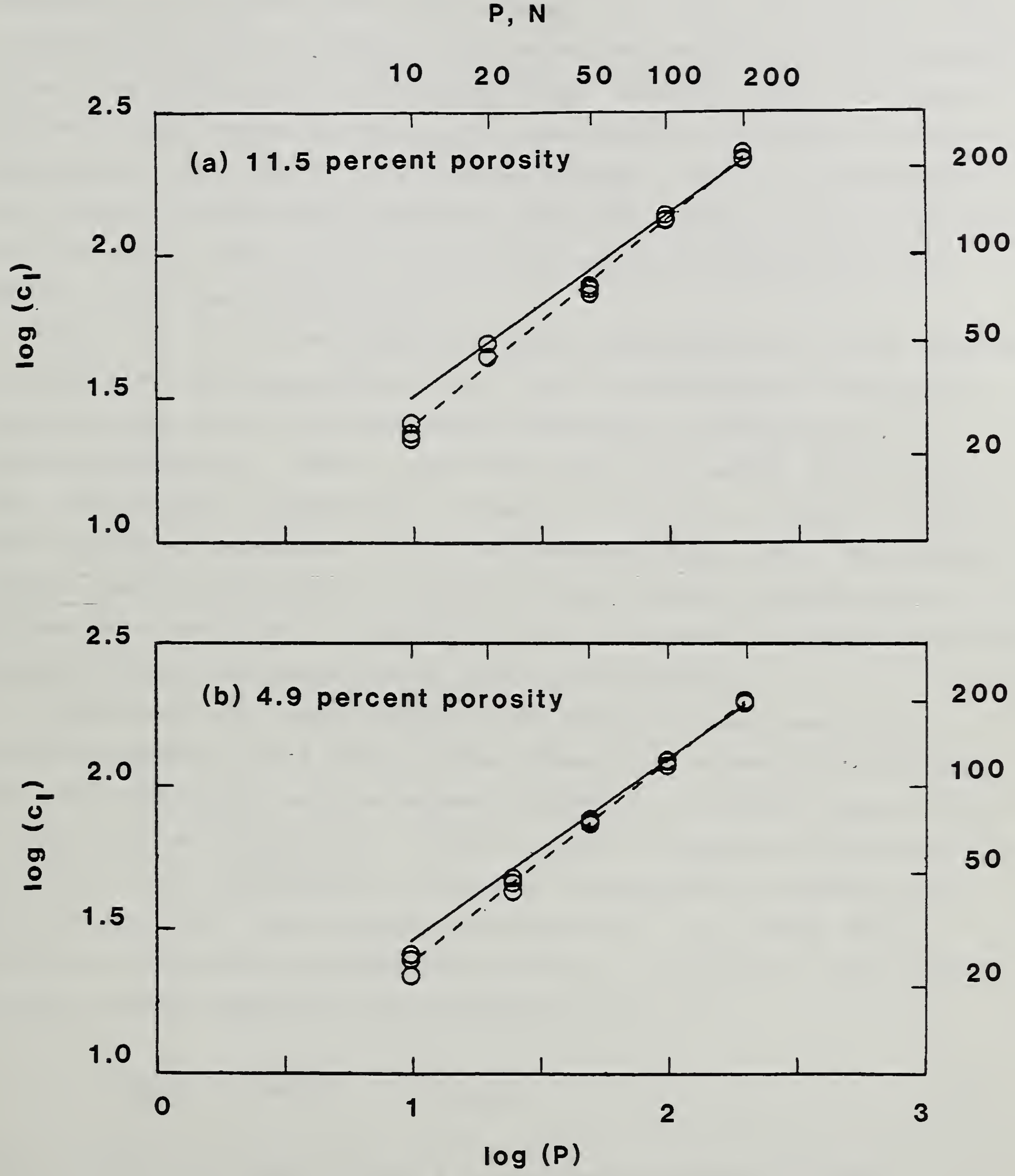

Figure 10. Half-length of surface crack, c_I, as a function of indentation load, P, for silicon carbide whisker reinforced alumina ceramics at selected porosities. The dashed line is a least-squares-fit, and the slope of the solid line is derived from the strength measurements.

However, evaluation of b from Eq. (17) is preferred because the variance of (1+b)/2 would have to be 0.25 of the variance of b from the slope of the strength data to provide the same variance of r. The solid lines in Fig. 10 describe the slope (1+b)/2 at the respective porosities of the material where b was deduced from the strength data. Clearly, there is a bias in the small crack region of indentation loads due to the failure to observe the complete crack length by optical microscopy. Thus, the coefficient A was evaluated as the mean logarithm of Eq. (20), using b from the strength data and the c_I only from the large crack region of indentation loads. Table 1 gives these values of A.

Since Eq. (17) is believed to provide a reasonable fit to the observed strength data, the supposition of Eq. (16) is confirmed as a reasonable representation of the crack-extension resistance of the materials at selected porosities. Table 1 gives the values of r and K_o deduced from Eqs. (18) and (19), respectively, using Y = 1.174 [11]. Figure 11 shows crack-extension resistance, K_R, as the function of Eq. (16). The shaded regions describe the range of critical stress-intensity factors that correspond to the onset of instability of crack extension deduced from the analysis for the two materials of selected porosities.

Analysis of the random errors in the strength measurements will elucidate whether or not the K_R curves themselves, appearing to increase with crack-extension, and the apparent difference in the K_R curves of the two materials are significant. Table 1 gives the standard deviations of b and log(C) for N measurements, following the statistical analysis of a straight line [12]. The standard deviations of r, K_o, and K_R were estimated by the law of propagation of errors. According to the principle of least squares applied to the logarithm of Eq. (17),

$$\mathrm{Log}(C) = \langle \log(S) \rangle + b \cdot \langle \log(P) \rangle \qquad (21)$$

where $\langle \log(S) \rangle = \Sigma \log(S_i)/N$ and P is assumed not subject to error. The variables $\langle \log(S) \rangle$ and b can be shown to be statistically independent [12], a necessary requirement for the validity of the law of propagation of errors. When Eqs. (18) through (21) are substituted in the logarithm of

Eq. (17), the standard deviation of $\log(K_R)$, reflecting only random errors in S, may be calculated as the square root of

$$\mathrm{var}[\log(K_R)] = \left[\frac{\partial \log(K_R)}{\partial\langle\log(S)\rangle}\right]^2 \mathrm{var}[\langle\log(S)\rangle] + \left[\frac{\partial \log(K_R)}{\partial b}\right]^2 \mathrm{var}(b) \qquad (22)$$

Table 1 gives the standard deviations of r and K_o, and Figure 11 shows the 90 percent confidence intervals for the materials, being approximately ± 4 and ± 3.4 percent over the range of measurements at the selected porosities, 11.5 and 4.9 percent, respectively.

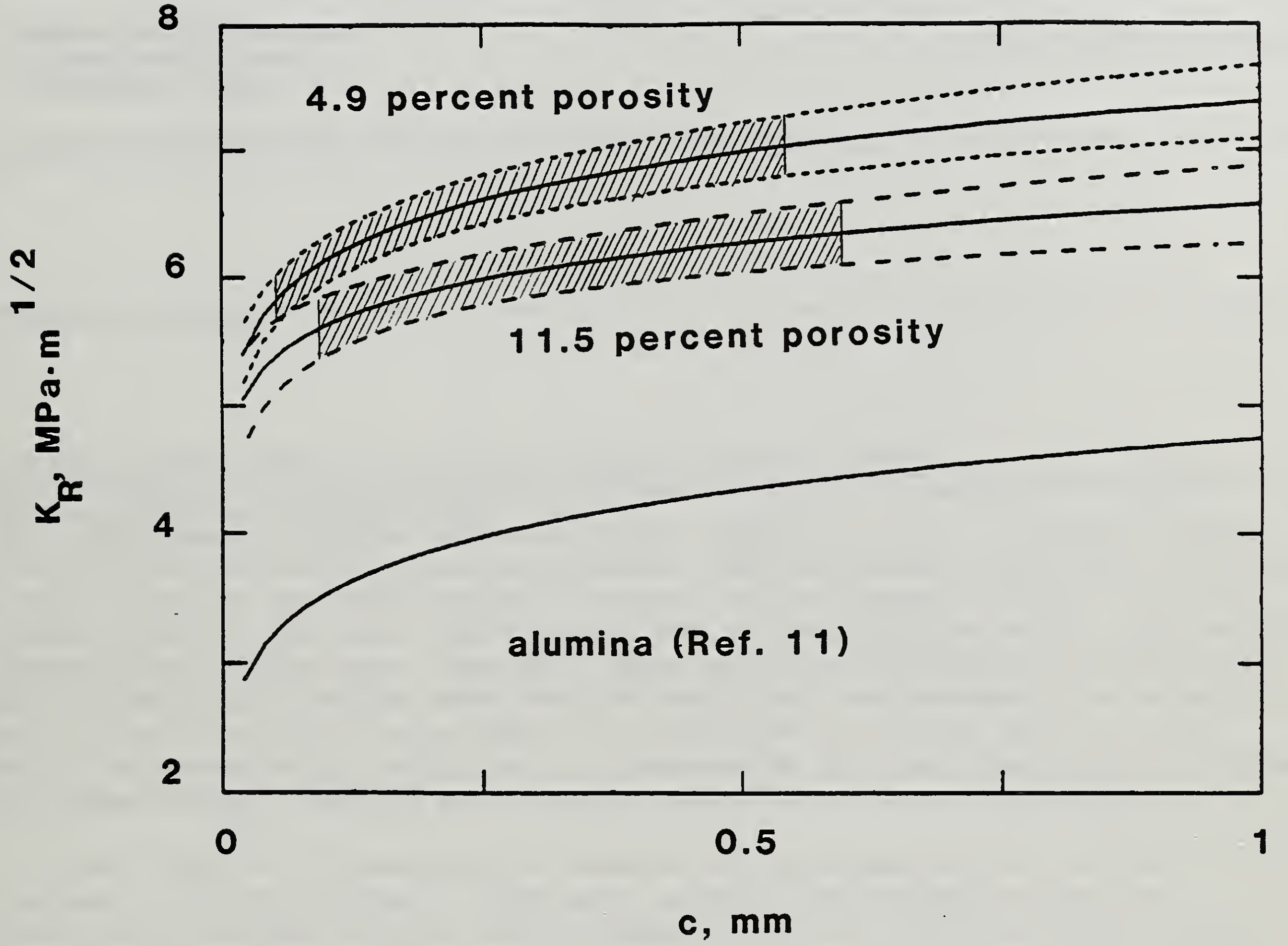

Figure 11. Crack-extension resistance, K_R, of silicon carbide whisker reinforced alumina ceramics at selected porosities compared to that of an alumina ceramic.

FORM NBS-114A (REV.11-84)

U.S. DEPT. OF COMM. **BIBLIOGRAPHIC DATA SHEET** *(See instructions)*	1. PUBLICATION OR REPORT NO. NBSIR 87-3564	2. Performing Organ. Report No.	3. Publication Date JUNE 1987

4. TITLE AND SUBTITLE

STRUCTURAL RELIABILITY AND DAMAGE TOLERANCE OF CERAMIC COMPOSITES FOR HIGH-TEMPERATURE APPLICATIONS

5. AUTHOR(S)

E. R. Fuller, Jr., T. W. Coyle, R. .F. Krause, Jr. and T.-J. Chuang

6. PERFORMING ORGANIZATION *(If joint or other than NBS, see instructions)*

NATIONAL BUREAU OF STANDARDS
U.S. DEPARTMENT OF COMMERCE
GAITHERSBURG, MD 20899

7. Contract/Grant No.

8. Type of Report & Period Covered

9. SPONSORING ORGANIZATION NAME AND COMPLETE ADDRESS *(Street, City, State, ZIP)*

NBS

10. SUPPLEMENTARY NOTES

☐ Document describes a computer program; SF-185, FIPS Software Summary, is attached.

11. ABSTRACT *(A 200-word or less factual summary of most significant information. If document includes a significant bibliography or literature survey, mention it here)*

The achievement of higher efficiency heat engines and heat recovery systems requires the availability of high temperature, high performance structural materials. Structural ceramics, and more recently, ceramic matrix composites have received particular attention for these applications due to their high strength, and corrosion and thermal shock resistance. Even with these positive attributes, improved reliability and extended lifetime under service conditions are necessary for structural ceramics to gain industrial acceptance. The problems with these materials are mechanical and chemical in nature and are enhanced by the fact that they are subjected to high temperatures, reactive environments and extreme thermal gradients.

With an objective of improved performance for heat engine/heat recovery applications, the NBS program on structural ceramics and ceramic composites addresses these problems through the determination of the critical factors which influence mechanical and microstructural behavior. The activities of the program are grouped under two major subtasks, each designed to develop key data, associated test methods and companion predictive models. The status of the subtasks are detailed in the following sections.

12. KEY WORDS *(Six to twelve entries; alphabetical order; capitalize only proper names; and separate key words by semicolons)*

composites; double-cleavage-drilled-compression; indentation; R-curve; SiC fibers; SiC whiskers; shear resistance; strength

13. AVAILABILITY

☒ Unlimited
☐ For Official Distribution. Do Not Release to NTIS
☐ Order From Superintendent of Documents, U.S. Government Printing Office, Washington, DC 20402.
☒ Order From National Technical Information Service (NTIS), Springfield, VA 22161

14. NO. OF PRINTED PAGES

30

15. Price

$11.95